



**HAL**  
open science

## Impact of droplets onto surfactant-laden thin liquid films

C.R. Constante-Amores, L. Kahouadji, S. Shin, J. Chergui, D. Juric, J.R.  
Castrejón-Pita, O.K. Matar, A.A. Castrejón-Pita

### ► To cite this version:

C.R. Constante-Amores, L. Kahouadji, S. Shin, J. Chergui, D. Juric, et al.. Impact of droplets onto surfactant-laden thin liquid films. 2022. hal-03808105v1

**HAL Id: hal-03808105**

**<https://hal.science/hal-03808105v1>**

Preprint submitted on 10 Oct 2022 (v1), last revised 23 Oct 2022 (v2)

**HAL** is a multi-disciplinary open access archive for the deposit and dissemination of scientific research documents, whether they are published or not. The documents may come from teaching and research institutions in France or abroad, or from public or private research centers.

L'archive ouverte pluridisciplinaire **HAL**, est destinée au dépôt et à la diffusion de documents scientifiques de niveau recherche, publiés ou non, émanant des établissements d'enseignement et de recherche français ou étrangers, des laboratoires publics ou privés.

# Impact of droplets onto surfactant-laden thin liquid films

C. R. Constante-Amores<sup>1,2†</sup>, L. Kahouadji<sup>2</sup>, S. Shin<sup>3</sup>, J. Chergui<sup>4</sup>, D. Juric<sup>4,5</sup>, J. R. Castrejón-Pita<sup>6</sup>, O. K. Matar<sup>2</sup>, A. A. Castrejón-Pita<sup>1</sup>

<sup>1</sup>Department of Engineering Science, University of Oxford, Oxford OX1 3PJ, UK

<sup>2</sup>Department of Chemical Engineering, Imperial College London, London SW7 2AZ, UK

<sup>3</sup>Department of Mechanical and System Design Engineering, Hongik University, KR

<sup>4</sup>Université Paris Saclay, Centre National de la Recherche Scientifique (CNRS), Laboratoire Interdisciplinaire des Sciences du Numérique (LISN), 91400 Orsay, France

<sup>5</sup>Department of Applied Mathematics and Theoretical Physics, University of Cambridge, Cambridge CB3 0WA, UK

<sup>6</sup>Department of Mechanical Engineering, University College London, WC1E 7JE, United Kingdom

(Received xx; revised xx; accepted xx)

We study the effect of insoluble surfactants on the impact of surfactant-free droplets on surfactant-laden thin liquid films via a fully three-dimensional direct numerical simulations approach that employs a hybrid interface-tracking/level-set method, and by taking into account surfactant-induced Marangoni stresses due to gradients in interfacial surfactant concentration. Our numerical predictions for the temporal evolution of the surfactant-free crown are validated against the experimental work by Che & Matar (2017). We focus on the ‘crown-splash regime’, and we observe that the crown dynamics evolves through various stages: from the the growth of linear modes (through a Rayleigh-Plateau instability) to the development of nonlinearities leading to primary and secondary breakup events (through droplet shedding modulated by an end-pinching mechanism). We show that the addition of surfactants does not affect the wave selection via the Rayleigh-Plateau instability. However, the presence of surfactants play a key role in the late stages of the dynamics as soon as the ligaments are driven out from the rim. Surfactant-induced Marangoni stresses delay the end-pinching mechanisms to result in longer ligaments prior to their capillary singularity, while also promoting the spanwise merging between ligaments. In addition, we show that the addition of surfactants leads to surface rigidification and consequently to the retardation of the flow dynamics.

## 1. Introduction

Droplets impacting on liquid surfaces are observed in a broad range of natural phenomena and industrial applications. Consequently, its study is driving a significant scientific interest; for comprehensive reviews please see e.g., Yarin (2006); Josserand & Thoroddsen (2016); Cheng *et al.* (2022). The complex topological features of droplet impact have attracted the fluid mechanics community since the first ground-breaking experiments from Worthington (1908) and Edgerton (1977) over a century ago. However, it was not until the advent of high-speed imaging and high-resolution computational tools that it became possible to capture the early dynamics of the broad range of scales involved in

† Email address for correspondence: crc15@ic.ac.uk

such phenomena (Thoroddsen 2002; Thoraval *et al.* 2012; Zhang *et al.* 2012; Agbaglah & Deegan 2014; Josserand *et al.* 2016; Thoroddsen *et al.* 2012; Fudge *et al.* 2021).

The dynamics of droplet impact on liquids is extremely diverse and is determined by a wide number of factors including the impact speed and the fluid properties, as well as whether the impact occurs on either a deep pool or a thin layer of fluid (Josserand *et al.* 2016; Deegan *et al.* 2007; Che & Matar 2017). At high impact speeds, the latter situation results in the formation of an upward Worthington jet (Gekle & Gordillo 2010), whereas the former case gives rise to the well-known *Milkdrop Coronet*, which is the subject of this paper (Deegan *et al.* 2007; Josserand *et al.* 2016; Thoroddsen 2002). Instants after impact on to a thin liquid layer, inertia prompts the formation of an ejecta sheet. After some time, its edge forms a capillary-driven cylindrical-shaped rim that evolves through various stages: first, a combination of Rayleigh–Taylor and Rayleigh–Plateau instabilities growth on the rim (see Agbaglah *et al.* (2013); Zhang *et al.* (2010)), to then develop non-linearities leading to breakup (through end-pinching, see Wang & Bourouiba (2018)), and the formation of a cascade of droplet sizes.

In fact, Deegan *et al.* (2007) presented a phenomenological picture of the interfacial dynamics in terms of a phase diagram in the  $We - Re$  space (here,  $We$  and  $Re$  stand for the Weber and Reynolds numbers, which represent the ratio of inertia to surface tension forces and inertia to viscous forces, respectively). In the ‘Peregrine-sheet regime’, i.e. low  $Re$  and moderate  $We$ , and high  $Re$  and low  $We$ , the dynamics are characterised by the generation of an axisymmetric ejecta sheet and rim. In the ‘crown-splash regime’, i.e. for low  $Re$  and high  $We$ , the rim undergoes longitudinal instabilities to trigger the formation of droplets. In the ‘microdroplet-splash regime’, i.e. for high  $Re$  and moderate  $We$ , fast and diminutive droplets are formed from the ejecta sheet immediately upon impact. Microdroplet-splash and crown-splash regimes are expected for high  $Re$  and high  $We$ .

Under most natural or industrial conditions, streams are contaminated with surfactants (i.e., surface-active agents), whose concentration variations lead to surface tension gradients, which in turn, result in the formation of Marangoni stresses and surface viscosities (see Manikantan & Squires (2020)). Previous studies have demonstrated the role of surfactants in capillary singularities (see for instance, Ananthkrishnan & Yeung (1994), Craster *et al.* (2002), Liao *et al.* (2004), Kamat *et al.* (2018) and Constante-Amores *et al.* (2020a)); here, we study the role of surfactant-induced flows on the late stages of splashing. Che & Matar (2017) demonstrated the role of surfactants on the impact dynamics onto thin liquid films for low and moderate Weber and high Reynolds numbers, e.g.,  $2.6 < We < 532$  and  $3000 < Re < 8654$ , respectively. In this past work, the authors showed that the presence of surfactants affect the post-impact dynamics such as the propagation of capillary waves, the growth of the crown, and the generation of secondary droplets. However, Marangoni stresses, surfactant concentration dynamics and other important insights of the impact phenomena were not investigated.

The vast majority of past works have focused on the physical understanding of the early dynamics of the ejected sheet using axisymmetric simulations, which is a valid assumption in the limiting case of  $t \ll D/U$  (where  $t$ ,  $D$ , and  $U$  stand for the time, the droplet diameter, and its characteristic velocity, respectively) – see for example Josserand & Zaleski (2003); Josserand *et al.* (2016); Agbaglah & Deegan (2014). In contrast, the study of the crown-splash regime requires the use of full three-dimensional (3D) numerical simulations in order to accommodate the natural occurrence of possible symmetry-breaking events, such as, the growth of transversal instabilities in the rim, or rim breakup into droplets. However, 3D simulations still remain a numerical challenge

(Gueyffier & Zaleski 1998) and have not often been reported in the literature, (Liang *et al.* 2019; Reijers *et al.* 2019; Chen *et al.* 2020; Xavier *et al.* 2020).

The present study aims to unravel the role of surfactant-induced Marangoni stresses on the interfacial dynamics during the impact of a surfactant-free droplet on a surfactant-laden thin layer of the same liquid in the crown-splash regime. Here, we perform 3D calculations of splashing in the presence of surfactants by using a hybrid front-tracking method to track the interface location. Section 2 presents the governing dimensionless parameters, the problem geometry, initial and boundary conditions, and the numerical validation. Section 3 provides a discussion of the results and concluding remarks are given in Section 4.

## 2. Problem formulation and numerical method

High resolution simulations were performed by solving the two-phase incompressible Navier-Stokes equations with surface tension in a three-dimensional Cartesian domain  $\mathbf{x} = (x, y, z)$  (see figure 1a). The interface between the gas and liquid is described by a hybrid front-tracking/level-set method, where surfactant transport is resolved at the interface (Shin *et al.* 2018). Here, and in what follows, all variables are made dimensionless (represented by tildes) using

$$\tilde{\mathbf{x}} = \frac{\mathbf{x}}{D_o}, \quad \tilde{t} = \frac{t}{t_r}, \quad \tilde{\mathbf{u}} = \frac{\mathbf{u}}{U}, \quad \tilde{p} = \frac{p}{\rho U^2}, \quad \tilde{\sigma} = \frac{\sigma}{\sigma_s}, \quad \tilde{\Gamma} = \frac{\Gamma}{\Gamma_\infty}, \quad (2.1)$$

where,  $t$ ,  $\mathbf{u}$ , and  $p$  stand for time, velocity, and pressure, respectively. The physical parameters correspond to the liquid density  $\rho_l$ , liquid viscosity,  $\mu_l$ , surface tension,  $\sigma$ , surfactant-free surface tension,  $\sigma_s$ , and  $U$  is the drop impact velocity, and  $D_o$  its initial diameter; hence, the characteristic time scale is  $t_r = D_o/U$ . The interfacial surfactant concentration,  $\Gamma$ , is scaled by the saturation interfacial concentration,  $\Gamma_\infty$ . As a result of this scaling, the dimensionless equations read

$$\nabla \cdot \tilde{\mathbf{u}} = 0, \quad (2.2)$$

$$\begin{aligned} \tilde{\rho} \left( \frac{\partial \tilde{\mathbf{u}}}{\partial \tilde{t}} + \tilde{\mathbf{u}} \cdot \nabla \tilde{\mathbf{u}} \right) + \nabla \tilde{p} = & - \frac{\mathbf{i}_z}{Fr^2} + \frac{1}{Re} \nabla \cdot [\tilde{\mu} (\nabla \tilde{\mathbf{u}} + \nabla \tilde{\mathbf{u}}^T)] + \\ & + \frac{1}{We} \int_{\tilde{A}(\tilde{t})} (\tilde{\sigma} \tilde{\kappa} \mathbf{n} + \nabla_s \tilde{\sigma}) \delta(\tilde{\mathbf{x}} - \tilde{\mathbf{x}}_f) d\tilde{A}, \end{aligned} \quad (2.3)$$

$$\frac{\partial \tilde{\Gamma}}{\partial \tilde{t}} + \nabla_s \cdot (\tilde{\Gamma} \tilde{\mathbf{u}}_t) = \frac{1}{Pe_s} \nabla_s^2 \tilde{\Gamma}, \quad (2.4)$$

where the density and viscosity are given by  $\tilde{\rho} = \rho_g/\rho + (1 - \rho_g/\rho) \mathcal{H}(\tilde{\mathbf{x}}, \tilde{t})$  and  $\tilde{\mu} = \mu_g/\mu + (1 - \mu_g/\mu) \mathcal{H}(\tilde{\mathbf{x}}, \tilde{t})$  wherein  $\mathcal{H}(\tilde{\mathbf{x}}, \tilde{t})$  represents a Heaviside function, which is zero in the gas phase and unity in the liquid phase, while the subscript ‘ $g$ ’ designates the gas phase, and  $\tilde{\mathbf{u}}_t = (\tilde{\mathbf{u}}_s \cdot \mathbf{t}) \mathbf{t}$  is the tangential velocity at the interface in which  $\tilde{\mathbf{u}}_s$  represents the interfacial velocity, and  $\kappa$  is the curvature. The interfacial gradient is given by  $\nabla_s = (\mathbf{I} - \mathbf{nn}) \cdot \nabla$  wherein  $\mathbf{I}$  is the identity tensor and  $\mathbf{n}$  is the outward-pointing unit normal. In addition,  $\delta$  is a Dirac delta function, equal to unity at the interface and zero otherwise, and  $\tilde{A}(\tilde{t})$  is the time-dependent interface area. The dimensionless groups that appear in the governing equations are defined as

$$Re = \frac{\rho_l U D_o}{\mu_l}, \quad We = \frac{\rho_l U^2 D_o}{\sigma_s}, \quad Fr = \frac{U}{\sqrt{g D_o}}, \quad Pe_s = \frac{U D_o}{D_s}, \quad \beta_s = \frac{\Re T \Gamma_\infty}{\sigma_s}, \quad (2.5)$$

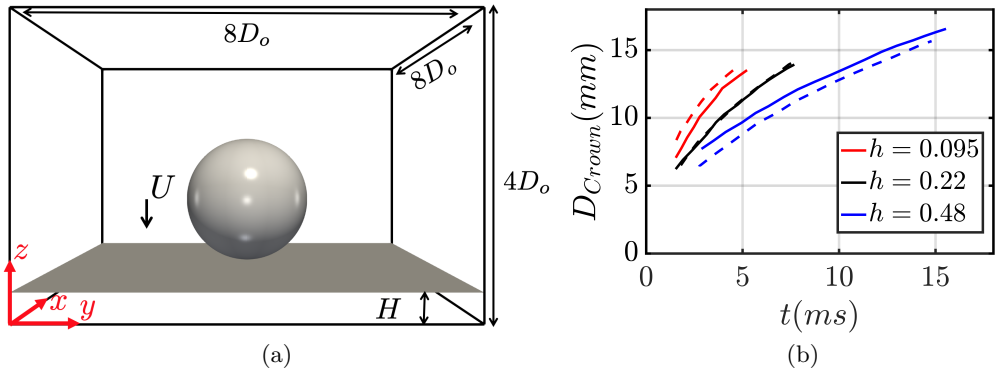


Figure 1: Schematic representation of the flow configuration, and validation of the numerical procedure: (a) initial configuration, highlighting the computational domain of size (not-to-scale)  $(8D_o \times 8D_o \times 4D_o)$  in a three-dimensional Cartesian domain,  $\mathbf{x} = (x, y, z)$ , with a resolution of  $772^3$ ; (b) validation of the numerical results (solid lines) against the experimental data (dashed lines) for the crown rim diameter temporal evolution of a surfactant-free case reported in Che & Matar (2017): effect of varying the dimensionless film depth,  $h = H/D_o$ , while keeping the other parameters constant ( $Re = 7514$ ,  $We = 249$ , and  $Fr = 186$ ).

where  $Re$ ,  $We$ ,  $Fr$ , and  $Pe_s$  stand for the Reynolds, Weber, Froude, and (interfacial) Peclet numbers. Gravity is negligible during the impact as indicated by the Froude number value, i.e.  $Fr \sim \mathcal{O}(10^2)$  (similar assumptions were made by Deegan *et al.* (2007)). The parameter  $\beta_s$  is the surfactant elasticity number that is a measure of the sensitivity of the surface tension,  $\sigma$ , to the interface surfactant concentration,  $\Gamma$ . The non-linear Langmuir equation is used to describe  $\sigma$  in terms of  $\Gamma$ , this is

$$\tilde{\sigma} = 1 + \beta_s \ln(1 - \tilde{\Gamma}). \quad (2.6)$$

The Marangoni stress,  $\tilde{\tau}$ , is expressed as a function of  $\tilde{\Gamma}$  as

$$\frac{1}{We} \nabla_s \tilde{\sigma} \cdot \mathbf{t} \equiv \frac{\tilde{\tau}}{We} = -\frac{Ma}{(1 - \tilde{\Gamma})} \nabla_s \tilde{\Gamma} \cdot \mathbf{t}, \quad (2.7)$$

where  $Ma = \beta_s/We = ReT\Gamma_\infty/\rho U^2 D_o$  is the Marangoni parameter and  $\mathbf{t}$  is the unit tangent to the interface. Here,  $\mathfrak{R}$  is the ideal gas constant value ( $\mathfrak{R} = 8.314 \text{ J K}^{-1} \text{ mol}^{-1}$ ),  $\mathcal{T}$  denotes temperature, and  $\mathcal{D}_s$  stands for the interfacial diffusion coefficient. Finally, a dimensionless thickness of the liquid layer,  $h = H/D_o$  is defined as the ratio between the liquid film thickness and the droplet diameter. Tildes are dropped henceforth.

### 2.1. Numerical Setup, validation and parameters

Figure 1a shows geometry and the initial and boundary conditions of the problem which closely follows previous work by Josserand *et al.* (2016); Agbaglah & Deegan (2014), and Fudge *et al.* (2021). A drop of initial size  $D_o$  with velocity  $U$  impacts a uniform layer of thickness  $H$  of the same liquid. The size of the computational domain is  $8D_o \times 8D_o \times 4D_o$ , which is sufficiently large to avoid any effects of artificial reflections from the boundaries. The centre of the drop is located at a small distance above the pool surface (e.g., an initial separation of  $0.05D_o$ ). A no-slip boundary is assumed for the bottom wall of the domain, whereas a no-penetration boundary condition is prescribed

for the top and lateral domain boundaries (similar to previous work by Batchvarov *et al.* (2020a)).

Figure 1b illustrates the ability of the numerical technique to reproduce the temporal evolution of the crown experimentally obtained and reported by Che & Matar (2017). After impact, inertia drives the rapid ejection of a vertical sheet from the pool, then capillarity prompts the formation of a rim, and then a crown. We observe excellent agreement for  $h = 0.22$ , while a small offset is observed for other two film thicknesses. The discrepancy could be attributed to conditions found in experimental conditions but not considered here, such as the surface waves produced during drop formation or air-induced flows during droplet fall. Nonetheless, the agreement between the numerical method and experimental results is visible. The numerical technique has also been validated for drop-interface coalescence, which can be considered as a limiting case of drop impact onto a pool, i.e.,  $U = 0$  (see Constante-Amores *et al.* (2021) for more details). The nonlinear interfacial dynamics have been validated for the capillary breakup of liquid threads (see Constante-Amores *et al.* (2020a, 2021) for more details). The numerical validation of the surfactant equations has been previously presented in Shin *et al.* (2018).

In terms of mesh resolution, we have ensured that our numerical simulations are mesh independent, and as a consequence, the numerical findings do not change by decreasing the cell size for a resolution of  $(772)^3$ . Additionally, liquid volume and surfactant mass conservation are met under errors of less than  $10^{-2}\%$ , and  $10^{-2}\%$ , respectively. Extensive mesh studies for surface-tension-driven phenomena using the same computational method can be found elsewhere, e.g. (Batchvarov *et al.* 2020a,b; Constante-Amores *et al.* 2020a, 2021, 2022).

The dimensionless values for the investigated phenomenon are consistent with experimentally realisable systems. We assume a water-air system, where the density and viscosity ratios are  $\rho_g/\rho_l = 1.2 \times 10^{-3}$  and  $\mu_g/\mu_l = 0.018$ , respectively. The targeted flow conditions for the surfactant-free base case are based on Deegan *et al.* (2007) who built a phase diagram in the  $We - Re$  space for  $h = 0.2$ . Our study focuses on the ‘crown-splash’ regime (i.e.,  $We > 500$  and  $Re < 1100$ ), as we aim to stay away from the ‘microdroplet-splash’ regime (i.e.,  $We > 500$  and  $Re < 1000$ ). The latter regime is characterised by the formation of a rapid ejecta sheet which undergoes capillary singularities to form microdroplets, requiring an extremely large resolution to capture droplet formation from the ejecta sheet and from the crown. Thus, we have selected  $Re = 1000$  and  $We = 800$  as the targeted surfactant-free case.

We have examined the case of adding surfactant to the thin liquid film but not the impacting droplet as it is less challenging to control the characteristics of surfactant-free drops experimentally. We have considered insoluble surfactants whose critical micelle concentration (CMC), i.e.  $\Gamma_\infty \sim \mathcal{O}(10^{-6})$  mol m $^{-2}$  for NBD-PC (1-palmitoyl-2-12-[(7-nitro-2-1,3-benzoxadiazol-4-yl)amino]dodecanoyl-sn-glycero-3-phosphocholine); thus, we have explored the range of  $0.1 < \beta_s < 0.9$  which corresponds to  $\mathcal{O}(10^{-7}) < \text{CMC} < \mathcal{O}(10^{-6})$  mol m $^{-2}$ , for typical values of  $\sigma_s$ . We have set  $Pe_s = 10^2$  following Batchvarov *et al.* (2020b) and Constante-Amores *et al.* (2020a) who showed that the interfacial dynamics are weakly-dependent on  $Pe_s$  beyond this value.

For a water-droplet of a typical size of  $D_o \sim \mathcal{O}(10^{-3})$ m, the impact time scale  $T_{imp} = t_r = D_o/U \sim \mathcal{O}(10^{-4} - 10^{-3})$ s; whereas the Marangoni time-scale  $T_\tau$  can be estimated by a balance between the Marangoni and the viscous stresses, resulting in  $T_\tau \sim \mu D^2/(h\Delta\sigma) \sim \mathcal{O}(10^{-4} - 10^{-3})$ s (see Che & Matar (2017) for more details). Therefore, surfactant-induced Marangoni stresses will play a crucial role in the flow physics. A discussion of the results is presented next.

### 3. Results

First, we discuss the early-time dynamics of the surfactant-free impact at  $Re = 1000$  and  $We = 800$ . Figure 2a shows the three-dimensional representation of the interface in the  $x - z$  plane ( $y = 4D_0$ ) at early times, i.e. prior transversal instabilities grow at the rim. As seen, instants after impact, we observe the formation of an axisymmetric thin layer of ejecta fluid which draws fluid from the droplet eventually giving rise to a *Peregrine sheet*, in agreement with Deegan *et al.* (2007) and Josserand *et al.* (2016). As time evolves, the Peregrine sheet grows upwards and expands radially while its film thickness reduces, here the radial coordinate  $r$  is defined at the initial point of impact. A closer inspection of the interfacial shape of the ejecta sheet at  $t = 0.5$  shows that its orientation is nearly horizontal, i.e. parallel to the pool. We also see surface tension forces inducing the formation of a hemispherical tip at the edge of the ejecta which leads to a pressure gradient between the tip and the adjacent sheet. The pressure gradient results in fluid motion from the tip towards the sheet. This behaviour leads to the formation of a sheet perpendicular to the pool at longer times; this in agreement with the experimental observations by Zhang *et al.* (2010) and Deegan *et al.* (2007). As the rim elongates to form the crown, we observe the grow of a azimuthal instability on the surface. Our results indicate that these naturally-occurring rim instabilities *select* wavelengths that are consistent with the most unstable Rayleigh-Plateau (RP) instability.

Here, we measured the average distance ( $\lambda$ ) between the 'undulations' or crests seen along the rim. We then normalised the result by the most unstable Rayleigh-Plateau (RP) instability wavelength, given by  $\lambda^* = 2\pi/k = 9.016a_o$ , where  $k$  is the growth rate of the instability that grows the fastest. Figure 2b shows the selected wavelength as a function of the rim radius; for the cases studied here  $\lambda/\lambda^* = 1.0 \pm 0.1$ . These results are in agreement with experimental results from Zhang *et al.* (2010), and the theoretical and computational work from Agbaglah *et al.* (2013) and Constante-Amores *et al.* (2022). A closer inspection of the top panel of figure 2b shows that the interfacial corrugations are not always evenly distributed alongside of the rim. We observe large wavelengths which are the result of interference between adjacent instabilities or other random numerical perturbations (in practice, experiments also suffer from random noise).

Figures 3a-d show a three-dimensional representation of the temporal evolution of the interface, from the time instabilities begin to be visible to the time droplets breakup by end-pinching. At these longer times ( $t > 5$ ), the rim is not much affected by the dynamics occurring at the impacting point and interfacial RP instabilities trigger the development of ligaments (see figure 3a). With increasing time, liquid ligaments grow perpendicular to the rim resulting in a local pressure-gradient-induced flow from the ligament to the tip, triggering the formation of a capillary-induced blob and a neck (displayed on figure 3b). The neck thins and stretches, due to a capillary-driven flow, to eventually resulting in the capillary pinch-off of a drop (the well-known 'end-pinching' mechanism proposed by Stone & Leal (1989)), see figure 3c. We note that the interfacial dynamics closely resembles experimental observations by Zhang *et al.* (2010), Josserand & Zaleski (2003) and (Deegan *et al.* 2007), as well as the dynamics of retracting sheets reported by Wang & Bourouiba (2018) and Constante-Amores *et al.* (2022).

Next, we proceed to study the role of surfactants on the flow dynamics; as illustrated by figures 3e-p where we observe the droplet impact at various elasticity parameters  $\beta_s$ . As seen, regardless of the value of  $\beta_s$ , large surfactant concentration gradients are found on the outer interface of the ejecta sheet. This result supports the idea that the ejecta sheet is generated at the interface of the surfactant-laden pool. On the other hand, the inner interface of the ejecta sheet arises from the surfactant-free drop, i.e.  $\Gamma$  vanishes on

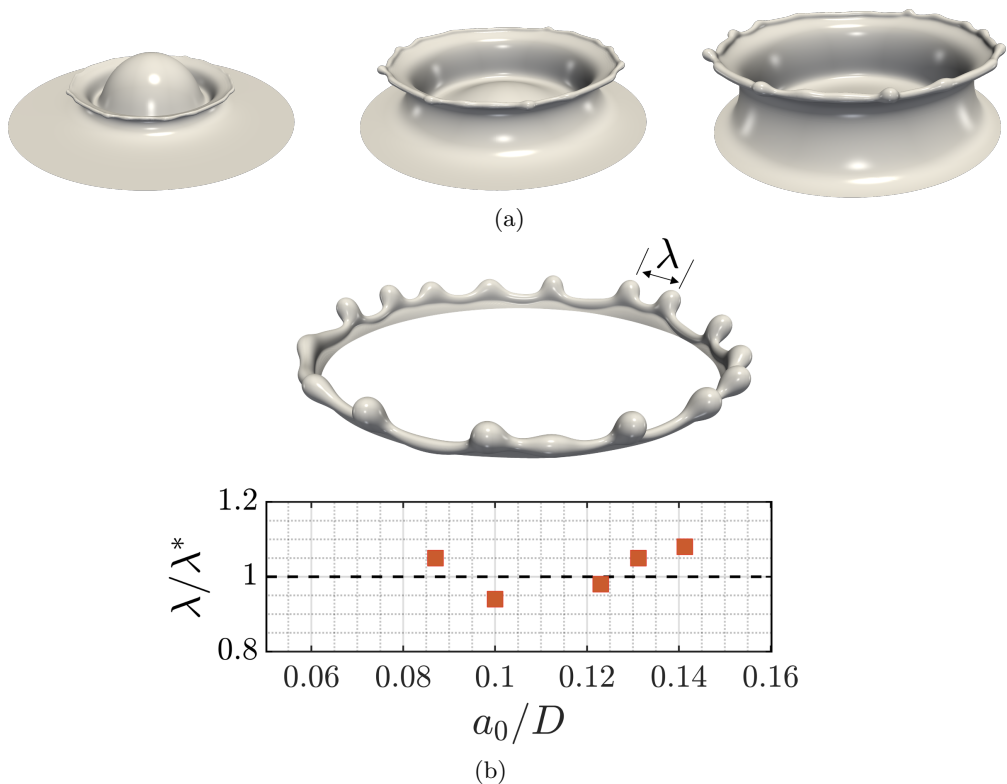


Figure 2: Wavelength selection in the crown splash regime. Panel (a) shows the early interfacial dynamics through a three-dimensional representation of the predicted interface location for  $Re = 1000$  and  $We = 800$ , at  $t = (0.5, 1.0, 1.5)$  corresponding to columns one to three, respectively. Panel (b) shows the selection of the wavelength  $\lambda$  normalized with the theoretical RP-instability,  $\lambda^*$ , at early times of the simulation for  $t < 7.5$ . A three-dimensional representation of the crown for the dimensionless time  $t = 7.5$  is also shown, highlighting the predicted wavelength between crests.

the inner surface, see figure 3e. This observation, that the fluid source of the inner and outer surfaces of the ejecta sheet are the pool and the droplet, respectively, is in good agreement with the work by Josserand *et al.* (2016). A close inspection of the distribution of  $\Gamma$  in the outer sheet shows that  $\Gamma$ -values are maximum at the base of the ejecta, and their values reduce upwards (see for example panel (e) of figure 3). This is the result of an increase of the interfacial area, that leads to a dilution of surfactant at the interface, thus the surfactant concentration (surface tension) decreases (increases). In addition, the interfacial expansion results in large convective effects that transport surfactant towards the rim; see figure 3e, in which larger values of  $\Gamma$  are found in the rim than in its adjacent sheet.

The increase (decrease) of  $\Gamma$  ( $\sigma$ ) implies that a large surface deformation is required to satisfy the normal stress balance at the interface. Similar to the surfactant-free case, capillary-induced flow results in the formation of a rim on the sheet edge, whose thickening leads to the onset of destabilisation. This is in agreement with previous studies from Asaki *et al.* (1995), who reported a surfactant-driven dampening effect on the capillary waves.

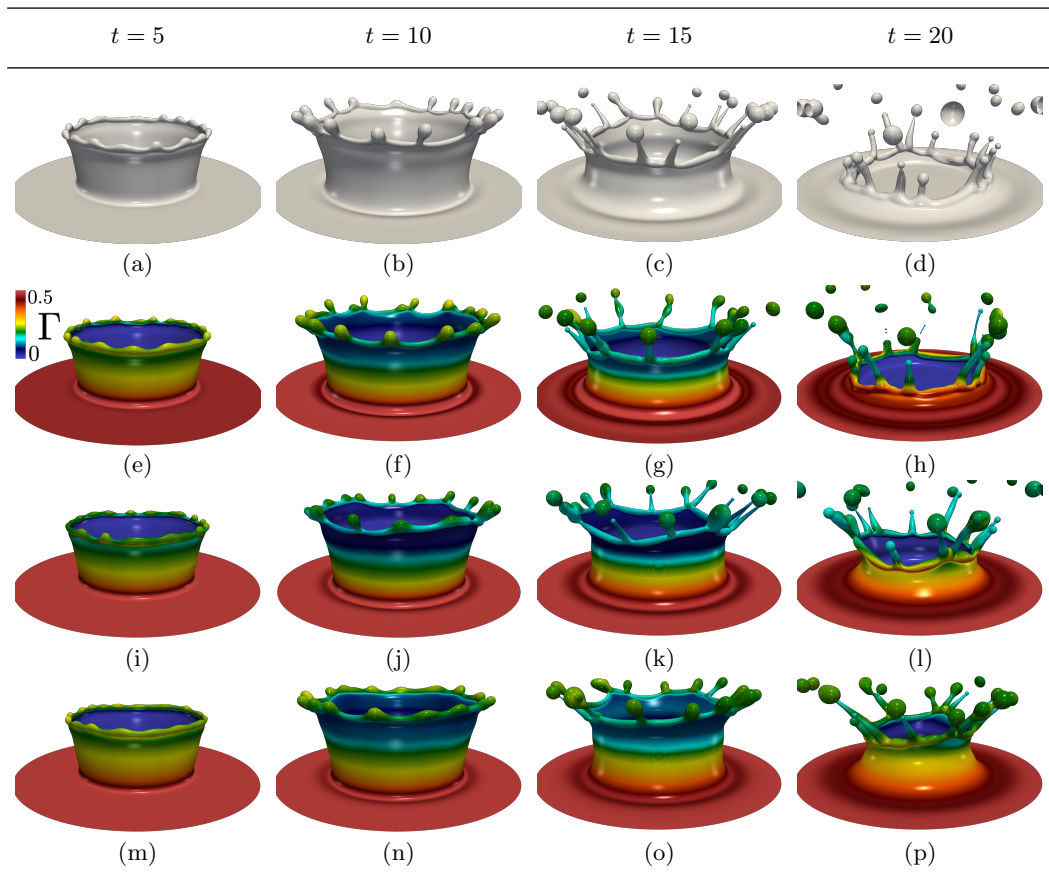


Figure 3: Effect of  $\beta_s$  on the drop impact dynamics for insoluble surfactants. Spatio-temporal evolution of the three-dimensional interface shape for surfactant-free cases, (a)–(d), and surfactant-laden cases for  $\beta_s = (0.1, 0.5, 0.7)$  corresponding to panels (e)–(h), (i)–(l) and (m)–(p), respectively. Here, the dimensionless parameters are  $Re = 1000$ ,  $We = 800$  and  $h=0.2$ . For the surfactant-laden cases,  $Pe_s = 100$  and  $\Gamma = \Gamma_\infty/2$ , the colour indicates the value of  $\Gamma$ , and the legend is shown in panel (e).

In addition, we expect higher (lower) values of  $\Gamma$  at the rim wave crests (instability waves) as they belong to a radially converging (diverging) region, which have the effect of locally increasing (reducing)  $\Gamma$ . The gradients in  $\Gamma$  result in surfactant-induced Marangoni stress flows from the higher- $\sigma$  radially diverging to the lower- $\sigma$  converging regions. This slows down the interfacial dynamics, and the formation of instabilities at the rim. Those findings are in agreement with Constante-Amores *et al.* (2022). By increasing  $\beta_s$  the surfactant distribution along the interface is enhanced, as displayed in figure 3i-l and figure 3j-m for  $\beta_s = 0.5$  and  $\beta_s = 0.7$ , respectively.

Surfactant-induced Marangoni stresses only delay the development of the ligament from the rim; these eventually end-pinch to form droplets, see figure 3f,g. These predictions agree well with the experimental observations of Che & Matar (2017). Figure 4 shows the selected instability wavelength in terms of  $\beta_s$  and  $a_0$ . Indeed, a close inspection indicates that the surfactant does not affect the selection of the wavelength; the predicted

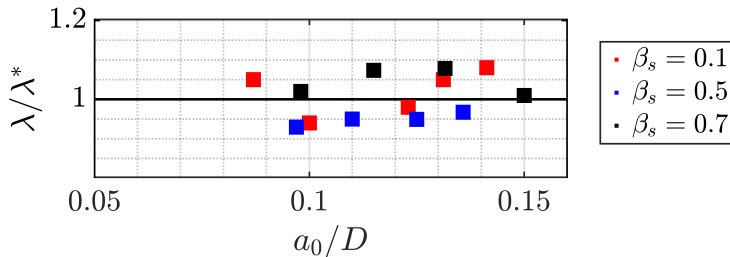


Figure 4: Effect of the elasticity parameter,  $\beta_s$  in the selection of wavelength of the undulations normalized with the theoretical RP instability,  $\lambda/\lambda^*$ , for  $t < 7.5$ .

$\lambda$  is consistent with the most unstable RP instability at a ratio of  $\lambda/\lambda^* = 1.0 \pm 0.1$ . Consequently, according to our results, the crown dynamics are mostly driven by the RP instability, although longer ligaments prior break up developed in the presence of surfactants, as observed in figure 3e. This indicates that Marangoni stresses promote the escape from end-pinching, as previously demonstrated by Constante-Amores *et al.* (2020a, 2022)

Two-dimensional projections, in the  $x-z$  plane ( $y = 4D$ ), of the interfacial shape,  $\Gamma$ ,  $\tau$ , and the radial component of the interfacial velocity  $u_{tz}$  in terms of  $\beta_s$  and a fixed value of  $Pe_s$ , are displayed in figures 5 and 6 corresponding to  $t = 5$  and  $t = 20$ , respectively. As described above, at early times, i.e.  $t = 5$ , drop impact results in a non-uniform interfacial surfactant distribution, with high surface concentrations at the base of the ejected sheet. As seen, the interfaces of the surfactant-free and the  $\beta_s = 0.1$  surfactant-laden cases are practically indistinguishable. However, as the surfactant concentration increases,  $\Gamma$  distributions trigger surfactant-driven dynamics from the sheet-base to its edge (see figure 5b). As  $\beta_s$  increases, long ejected sheets are promoted resulting in the reduction of the rim- and sheet-thickness due to mass conservation (displayed in the magnified panel of figure 5a). The increase in  $\beta_s$  also enhances the  $\Gamma$  distribution and increases the value of  $\tau$  (see the increase of  $\tau$  with  $\beta_s$  in figure 5c). Figure 5c shows the presence of large  $\tau$  peaks at both sides of the rim due to the accumulation of  $\Gamma$ , and suddenly drops at the base of the rim, suggesting a fluid transport from the rim to the sheet. In addition, a larger  $\tau$  maximum is observed from the side of the inner sheet as the inner sheet is devoid of  $\Gamma$  leading to an uneven flow motion inside the sheet. The variation of the streamwise interfacial tangential velocity  $u_{tz}$ , along the arc length, is shown in figure 5d. This figure, at early stages of the dynamics, sees  $u_t > 0$  over the majority of the domain due to the dominance of the vertical radial expansion of the ejecta sheet. A strong variation of  $u_{tz}$  is observed around the rim with  $u_{tz}$  tending to zero at a sufficiently large distance away from the impact region.

The influence of  $\beta_s$  at long times,  $t = 20$ , is examined in figure 6. Qualitatively, the surfactant effects are particularly evident as the dynamics have been slowed down by the surface rigidification brought by the Marangoni stresses, see figure 6a. As  $\beta_s$  decreases ( $\sigma$  increases), the surfactant is highly convected as  $\tau$  tends to zero, lowering the interfacial tension and consequently increasing surface deformation. As  $\beta_s$  increases, the gradient in  $\Gamma$  ( $\tau$ ) decreases (increases) near the rim, and the Marangoni stresses predominantly retard the flow and ‘rigidify’ the interface.

Figure 6c shows that the increase of  $\beta_s$  results in the strengthening of  $\tau$ , and consequently in a uniform  $\Gamma$  distribution. Figure 6d provides conclusive evidence of the

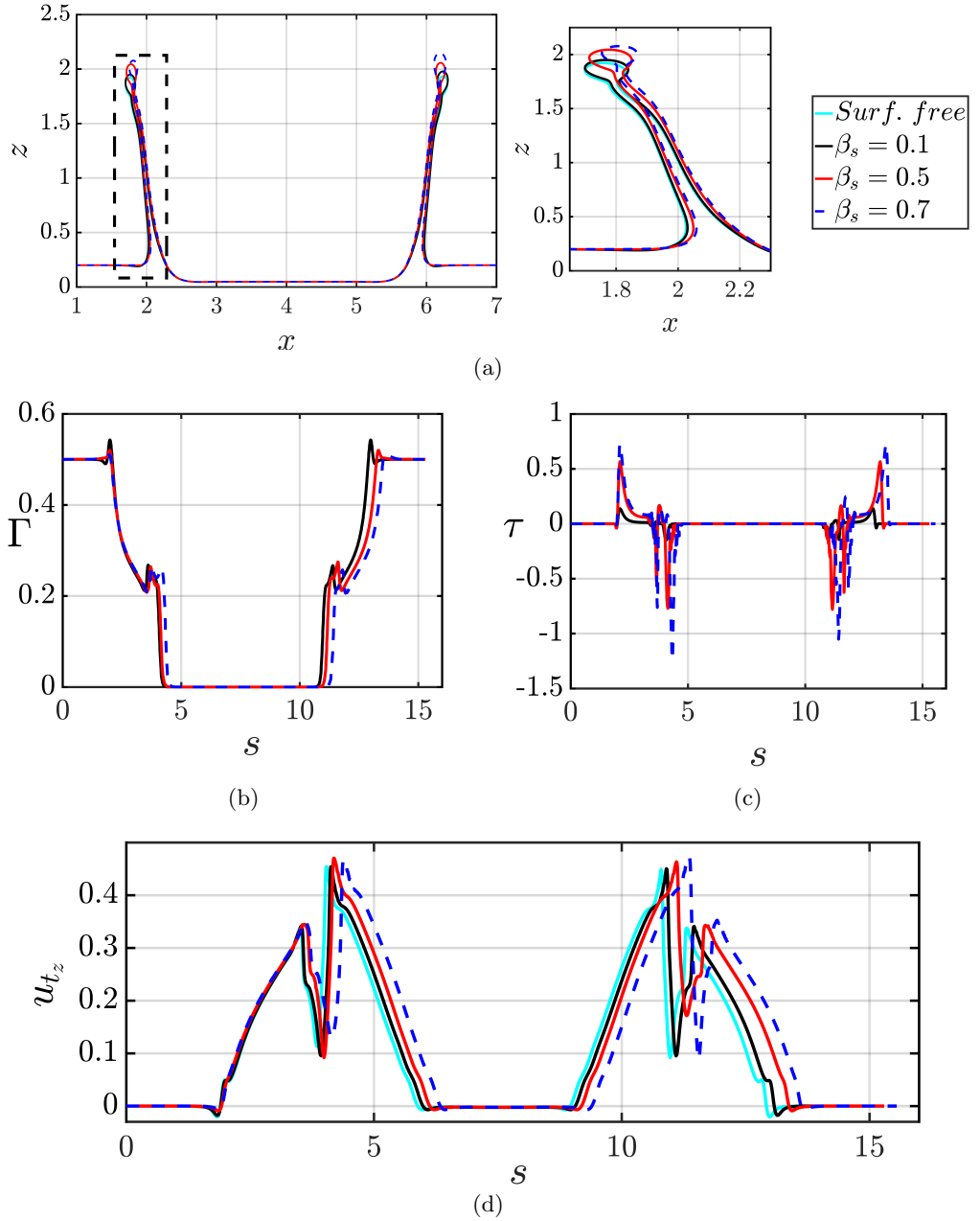


Figure 5: Effect of the elasticity parameter,  $\beta_s$ , on the flow dynamics at  $t = 5$ . Two-dimensional projections of the interface,  $\Gamma$ ,  $\tau$ , and  $u_{tz}$  in the  $x$ - $z$  plane ( $y = 4D$ ) are shown in (a) – (d), respectively. In panel (a), a magnified view of the ejecta sheet is also shown. Note that the abscissa in (a) corresponds to the  $x$  coordinate, and in (b) – (d) to the arclength,  $s$ . All parameters remain unchanged from figure 3.

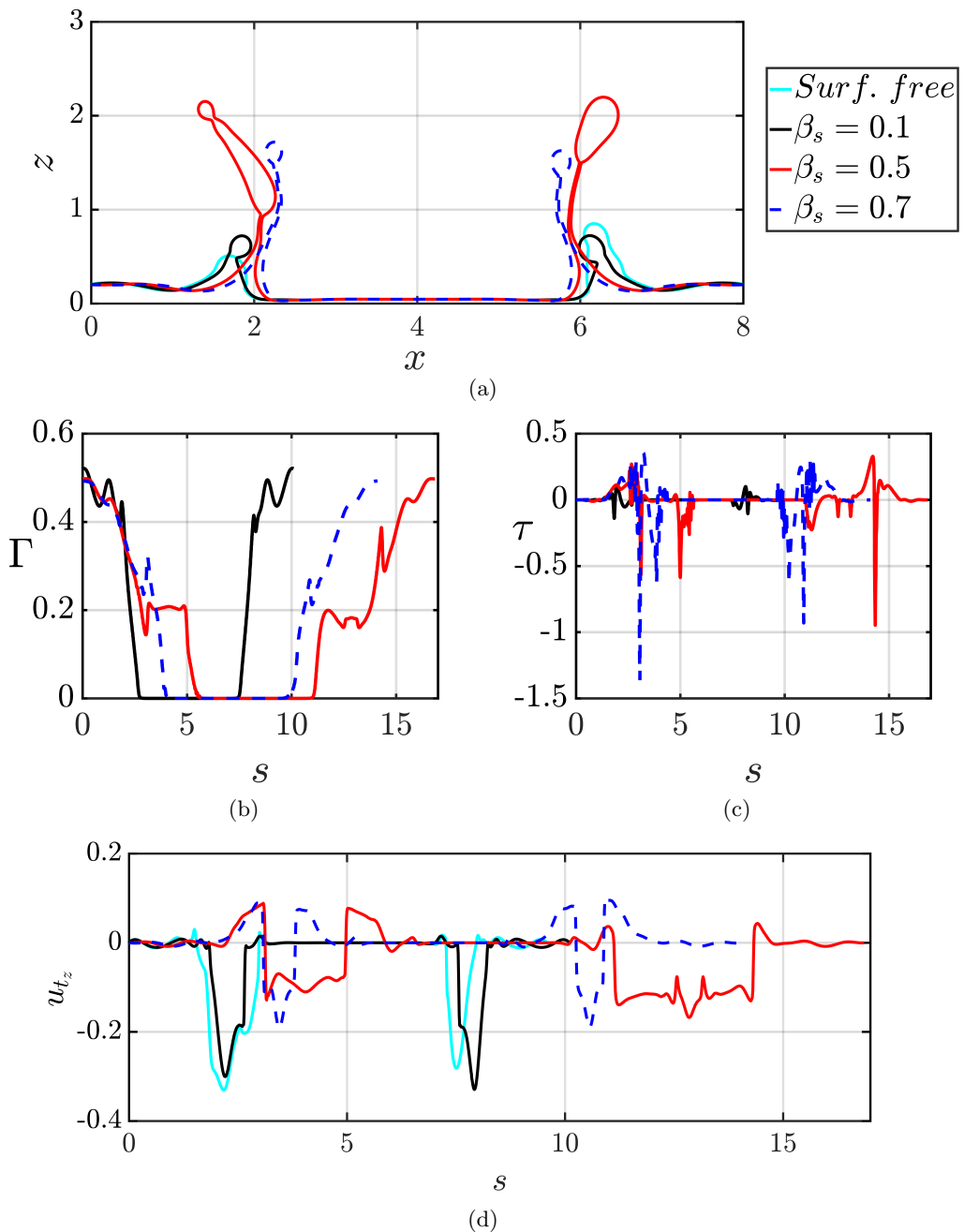


Figure 6: Effect of the elasticity parameter,  $\beta_s$ , on the flow dynamics at  $t = 20$ . Two-dimensional projections of the interface,  $\Gamma$ ,  $\tau$ , and  $u_{tz}$  in the  $x-z$  plane ( $y = 4D$ ) are shown in (a) – (d), respectively. Note that the abscissa in (a) corresponds to the  $x$  coordinate, and in (b) – (d) to the arclength,  $s$ . All parameters remain unchanged from figure 3.

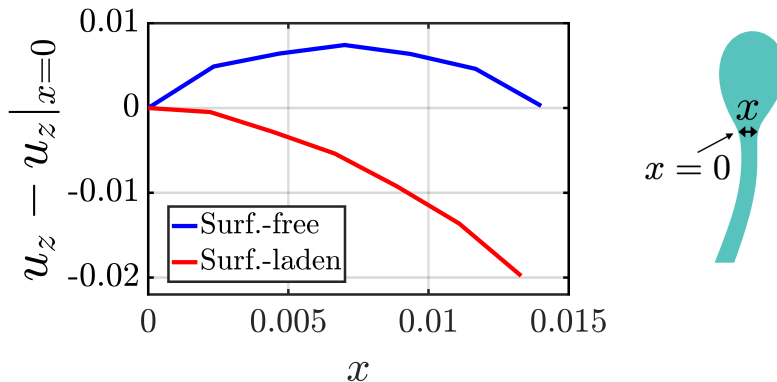


Figure 7: Profiles of the velocity component,  $u_z$ , in the sheet-normal direction inside the sheet for the surfactant-free and surfactant-laden ( $\beta_s = 0.5$ ) cases at  $t = 5$ . Here,  $u_z$  has been calculated in an inner-sheet frame-of-reference along the cross-stream direction,  $x$ , for the axial location indicated in the right panel. Note that the abscissa corresponding to  $x$  has been normalised with the initial location of the inner sheet. All parameters remain unchanged from figure 3.

surface rigidification as most of the  $u_{tz}$  is characterised by a negative value due to the decay of the dynamics. The variation of  $u_{tz}$  decreases as  $\beta_s$  increases, strengthening the Marangoni stresses arising from the surfactant-induced surface tension gradients. Finally, according to the foregoing results, we conclude that the interfacial dynamics for surfactant-laden cases in the ‘crown-regime’ resemble its surfactant-free counterpart except for the retardation due to the surface rigidification brought about by the presence of surfactant-induced Marangoni stresses.

Figure 7 shows component of the velocity variation in the sheet-normal direction,  $u_z$ , within the sheet, in a frame-of-reference moving with the inner-sheet at  $t = 5$ . For the surfactant-free case, the liquid within the sheet follows a parabolic profile into the rim; this effectively corresponds to a no-slip condition with  $u_z$  pinned to the interface, due to the absence of surfactants. In contrast, a predominantly shear-flow-like velocity profile is seen for the surfactant-laden case due to the absence of significant pressure gradients arising from the local interfacial curvature. Conclusively, figure 7 shows the outcome of the competition between capillary and Marangoni-driven flows (surfactant-induced tangential stresses on the outer rim wall) in the film near the rim:  $\tau$  triggers the deceleration of the fluid during the expansion of the crown.

Figure 8a shows the late stages of a surfactant-laden ligament before break up. A competition between viscosity and capillarity drives the formation of and dynamics of bulbous edge on the ligament tip. The relative importance of viscous to surface tension forces is calculated by the local Ohnesorge number for the ligament (i.e.  $Oh = \mu_l / \sqrt{\rho_l \sigma_s R}$ , here  $R$  stands for the average radius of the ligament), resulting in  $Oh \sim 0.07$ . Consequently, in the low  $Oh$ -regime, the local flow dynamics affecting the ligament (i.e., surfactant-driven escape from end-pinching) can be explained by the mechanism proposed by Constante-Amores *et al.* (2020a). Figures 8b,c and 8d,e show  $\Gamma$  and  $\tau$ , and the tangential velocity components  $u_t$  for the framed panels in figure 8a, respectively. Figure 8b,d show that, near the neck (marked with a blue diamond symbol)  $\tau$  results in  $u_{ty} > 0$  preventing the formation of the stagnation point required to trigger the capillary singularity. As shown by Constante-Amores *et al.* (2020a), two stagnation points

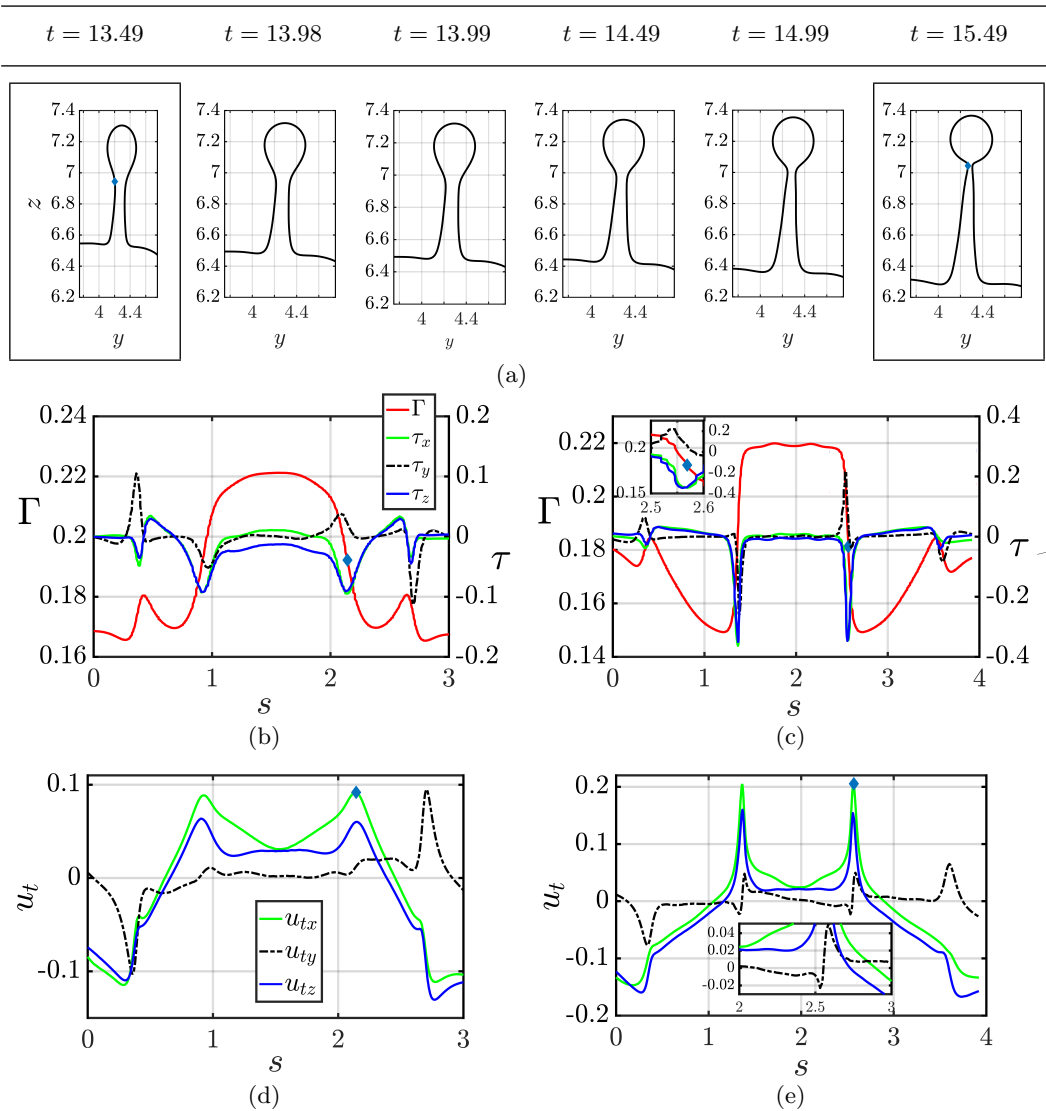


Figure 8: (a) Spatio-temporal evolution of a surfactant-laden ligament and its escape from pinchoff driven by surfactant-induced Marangoni flow when  $\beta_s = 0.5$ . (b) and (c) represent  $\Gamma$  and  $\tau$  as a function of the arclength  $s$  for the framed panels of (a), i.e.,  $t=13.49$  and  $t=15.49$ , respectively; (d) and (e) represent the tangential velocity  $u_t$  as a function of the arc length  $s$ . The red arrows in (b) and (c) represent the direction of Marangoni-induced flow, and the blue arrows in (d) and (e) highlight the direction of the flow driven by capillarity. The diamond markers represent the location of the neck. All parameters remain unchanged from figure 3.

sandwiched between the neck boundaries are needed to induce end-pinchng, as can be observed in 8d-e. Surface tangential stresses prevent capillary breakup for a longer time than in the surfactant-free case leading to longer ligaments and an increase in surface area. This results in the dilution (increase) of surfactant (surface tension) and the eventual

reduction in the strength of surfactant-induced Marangoni stresses thus initiating end-pinching.

Next, we focus on drop formation and the splash phenomena: we have identified three different modes of droplet shedding. The first mode corresponds to droplet detaching from the ligament via end-pinching. In the second mode we observe the initial ejection of filaments that are rapidly recombined into a single filament, see figure 10(a) to (e). The third mode sees the formation of satellite (smaller) droplets during the stretching of the filament neck. These satellite droplets are not observed for large values of the elasticity parameter, in agreement with Kovalchuk *et al.* (2018). For the surfactant-free case, figure 9, ligaments merge due to the presence of local cusps arising from a non-uniform distribution of mass per unit length (in agreement with Gordillo *et al.* (2014) and Wang & Bourouiba (2018)), or by the rim parameter not being a multiple of the RP instability. In the vicinity of a cusp, the rim is not perpendicular to the flow entering the rim; instead, it takes an angle,  $\theta$ , as shown in figure 9. This, oblique flow induces a local drift velocity in the longitudinal direction of the rim. In a reference frame along the rim, the drift velocity can be calculated from the projection of the incoming velocity  $u_{\text{in}}$  in the longitudinal direction of the rim as  $u_{\text{drift}} = u_{\text{in}}(t) \sin \theta$  (see Wang & Bourouiba (2018) for more details). Under the conditions of figure 9, we obtain  $u_{\text{drift}} \sim 0.106$  m/s and  $\theta \sim 20^\circ \pm 3^\circ$ . In contrast, from simulations, the velocity field yields  $u_{\text{in}} \sim 0.27$  m/s which leads to  $u_{\text{drift}} \sim 0.083$  m/s, and a good agreement with the direct measurement. The collision of the drifting protrusions results in the formation of a corrugated ligament (see figure 9e), which succumbs to end-pinching resulting in drop formation (not shown).

The presence of surfactant enhances the ligament-merging mode due to surfactant-driven Marangoni stresses that induce a local radial flow in the spanwise direction of the rim, and a radial shift of the ligament position along the rim. Figure 10 shows the temporal evolution of two protrusions that eventually become ligaments, and merge prior pinchoff. Figure 10a shows that the highest  $\Gamma$  values are found at the protrusions as they are characterised by regions of a radially converging dynamics, and subsequently, increased (i.e. reduced)  $\Gamma$  ( $\sigma$ ) locally. These results demonstrate that the effect of Marangoni stresses from adjacent protrusions is to bridge their gap promoting the collision and merging of the ligaments. Figure 10f shows a three-dimensional reconstruction of the  $|\tau|$  profile with respect to the arc-length,  $s$ , across a plane cutting the rim seen in 10a in half; the arrows represent the direction of  $|\tau|$  evidencing the enhancement of the filament merging. To the best of our knowledge, this surfactant-induced mechanism of droplet shedding has not been reported previously.

Figure 10 also shows that surfactant is highly convected from the rim to the film, resulting in the reopening of the film sheet. Consequently, the crown is thinner and survives longer in the presence of surfactants, in agreement with the experimental observations reported by Che & Matar (2017).

Next, we turn our attention to the size distribution of the droplets ejected from impact. Figure 11a shows the probability density function (PDF), at  $t = 20$ , scaled by the initial droplet diameter. It is important to note that as  $\beta_s$  increases, a higher droplet size is favoured. Figures 11b-d and 11e-g show the droplet volume, average surfactant concentration, and average velocity for each droplet at  $t = 15$  and  $t = 20$ , respectively. The average velocity and surfactant concentration are calculated as  $\langle |\mathbf{u}| \rangle = \int_{\Omega} |\mathbf{u}| d\Omega / \Omega$  and  $\langle \Gamma \rangle = \int_{\Omega} \Gamma d\Omega / \Omega$ , respectively, where  $\Omega$  represents the surface area of the droplet. We observe that the higher the value of  $\beta_s$  is, fewer droplets are produced due to the rigidification brought by surfactant-driven Marangoni stresses (see figure 11b,e). For the high values of  $\beta_s$ , we observe some droplets with large volume corresponding to the merging of ligaments. We also observe that small droplets are



Figure 9: Spatio-temporal evolution of two adjacent rim protrusions which shift in the spanwise direction induced by local cusps, resulting in their collision;  $\theta$  denotes the angle made by the right crest with the rim. The time difference between snapshots is  $\Delta t = 1.0$ . The parameters remain unchanged from figure 2.

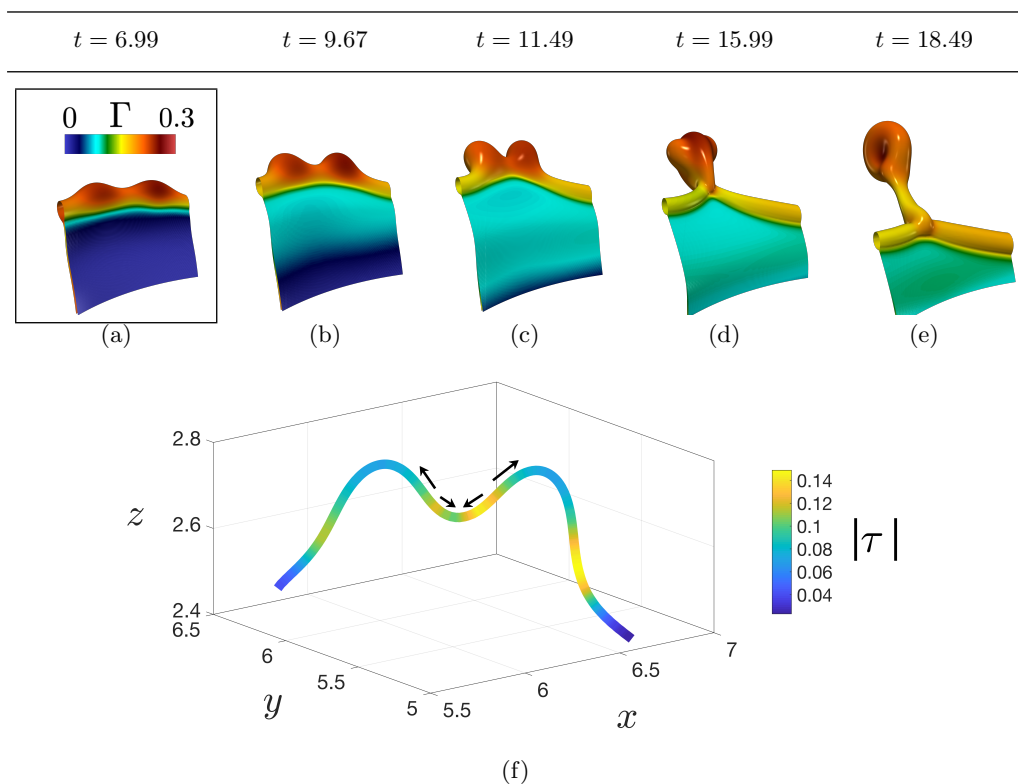


Figure 10: Spatio-temporal evolution of two adjacent rim protrusions shown panels (a) – (e) which shift in the spanwise direction due to surfactant-induced Marangoni stresses, resulting in their collision and merging. Panel (f) shows a three-dimensional reconstruction of the  $|\tau|$  profile with respect to the arc-length,  $s$ , across a plane cutting the rim in (a) in half; the arrows represent the direction of  $|\tau|$ . Here,  $\beta_s = 0.5$ , and all other parameters remain unchanged from figure 3.

produced for the surfactant-free and the  $\beta_s = 0.1$  surfactant-laden cases, (see figure 11e). These small droplets correspond to satellite droplets, which are characterised by  $V, < |\mathbf{u}| >$  and  $< \Gamma > \rightarrow 0$ , in good agreement with Kovalchuk & Simmons (2018) and Che & Matar (2017). We conclude that the addition of surfactants leads to a larger droplet

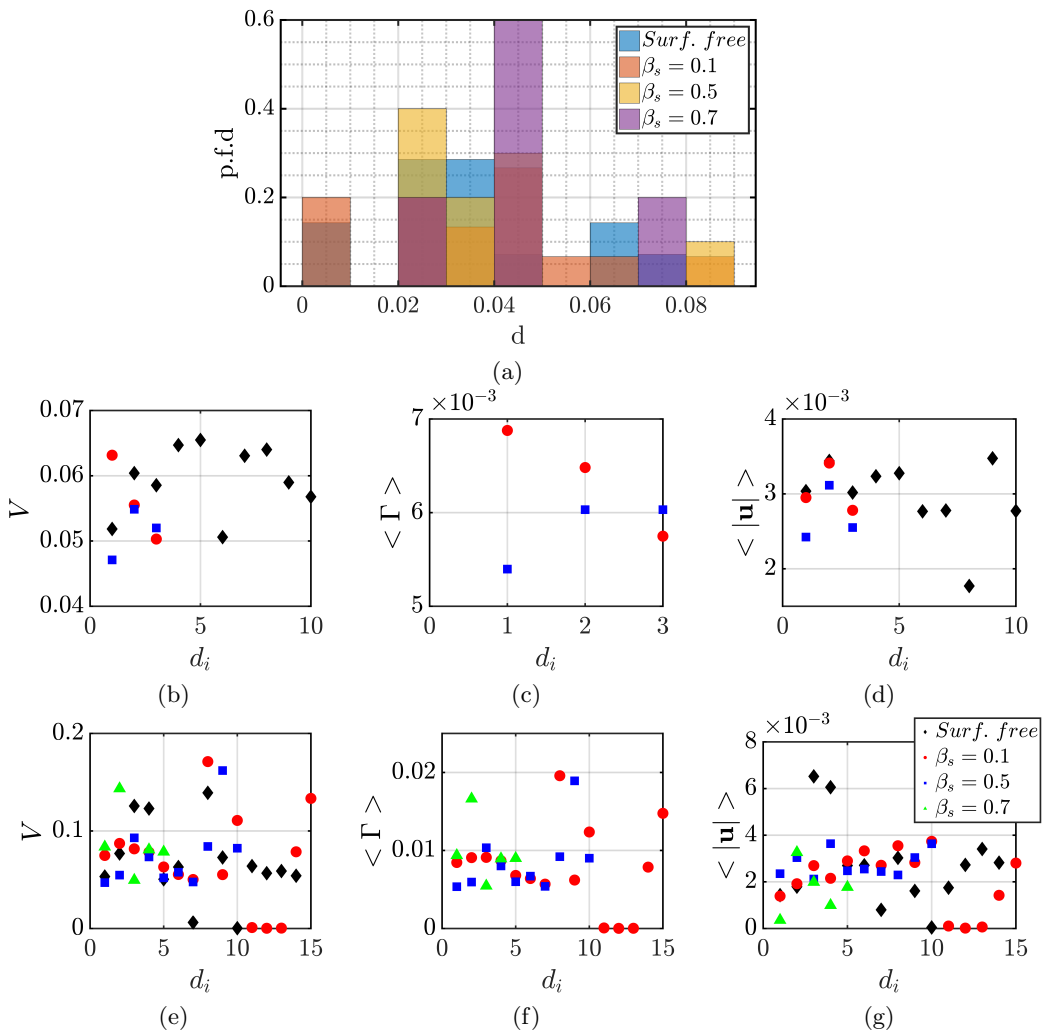


Figure 11: Metrics of splashing as a function of the elasticity parameter  $\beta_s$ . Panel (a) shows the probability density function (p.f.d) of the droplet size; droplet sizes are made dimensionless by the initial droplet diameter. Panels (b) – (d) and (e) – (g) show the volume, average surfactant concentration, and average velocity for every droplet at  $t = 15$ , and  $t = 20$ , respectively. All other parameters remain unchanged from figure 3.

size distribution for two reasons: the retardation of the dynamics, and the suppression of end-pinching through the reopening of the neck driven by a surfactant-induced flow.

Figures 11(c,f) show that the average  $\langle \Gamma \rangle$  of the droplets is lower than the surfactant concentration of the pool. This agrees well with the experimental studies of Blanchard & Syzdek (1972) and Constante-Amores *et al.* (2020b) on bursting bubbles. Figure 11c highlights that  $\langle \Gamma \rangle$  increases with decreasing  $\beta_s$  as the surfactant has been highly convected towards the rim. Lastly, figures 11(d,g), which show  $\langle |\mathbf{u}| \rangle$  at  $t = 15$  and  $t = 20$ , respectively, demonstrate the effect of rigidification brought about by surfactant-induced Marangoni flow which corresponds to an overall reduction in  $\langle |\mathbf{u}| \rangle$  for the surfactant-laden droplets.

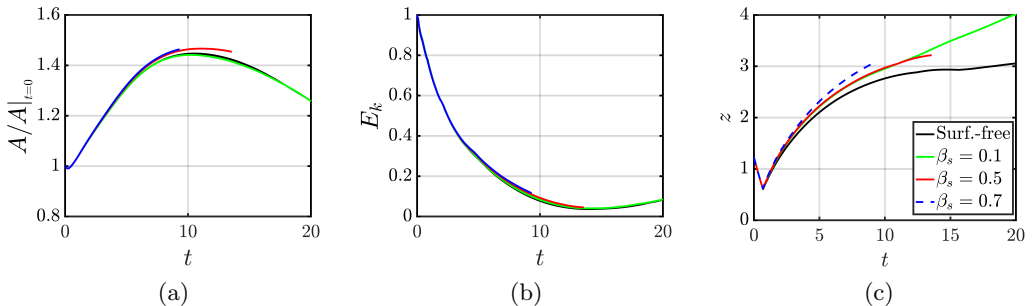


Figure 12: Temporal evolution of the total interfacial area, (a), and the kinetic energy, (b), normalised by their initial values, and the location of the sheet, (c), for the surfactant-free and surfactant-laden cases. All parameters remain unchanged from figure 3.

Figure 12a shows that after the drop, as  $\beta_s$  increases, a longer interface area is observed as surfactants rigidify the surface and stabilise the sheet. The peak of the interfacial area corresponds at  $t = 10$ , the moment of the destabilization of the rim due to RP instability. In fact, a reduction of the interfacial area is observed as soon as the sheet retracts. The kinetic energy plots indicate that the kinetic energy of the system is not much affected by the presence of the surfactant, which is explained by the dominance of inertial forces over surface tension.

#### 4. Concluding remarks

We have presented, for the first time, a detailed analysis of the effect of insoluble surfactants on the dynamics of droplet impact on thin-film liquid layers using high-resolution three-dimensional simulations. This article focuses on the crown-splash regime, in which the spanwise destabilisation of the rim leads to the formation of ligaments and droplets. Thus, we have focused on conditions of high Reynolds and Weber numbers. The nature of the hybrid front-tracking level-set numerical simulations enables the coupling, and analysis, of inertia, capillarity, interfacial diffusion, and Marangoni stresses owing to the presence of surfactant-induced surface tension gradients. According to our results, the addition of surfactants does not significantly affect the selection of the wavelength of the transversal rim instability; as the predicted wavelength is consistent with the most unstable Rayleigh-Plateau instability. The instability give rise to the formation of ligaments which eventually end-pinch into droplets. In the presence of surfactants, we observe a delay in endpinching, driven by surfactant-induced Marangoni stresses, resulting in longer ligaments. We identify three modes of droplet ejection, and show that surfactant-induced Marangoni stresses result in the bridging of the spanwise surfactant concentration gradients between consecutive ligaments in the rim, eventually leading to their merging. The presence of surfactant-induced Marangoni stresses also leads to interfacial rigidification, which is observed through a reduction of the surface velocity and the kinetic energy, and a larger interface area.

This research is of importance to many applications as droplet impact onto finite-depth liquid layers is found in a wide range of industrial and daily-life applications, from raindrops impinging onto puddles to screen and inkjet printing. This research focuses on the crown splashing regime, but we acknowledge that surfactants have a crucial role in other  $We - Re$  regions, e.g. at the microdroplet-splash regime. In fact, an interesting future line of study is to investigate the effect of the bulk solubility on the interfacial

flow dynamics. Additionally, surfactant-induced rheological effects could be important of great relevance to industry and most industrial fluids are formulated with dispersants (surfactants).

Declaration of Interests. The authors report no conflict of interest.

CRC-A and AAC-P acknowledge the support from the Royal Society through a University Research Fellowship (URF/R/180016), an Enhancement Grant (RGF/EA/181002) and two NSF/CBET-EPSRC grants (Grant Nos. EP/S029966/1 and EP/W016036/1). O.K.M. acknowledges funding from PETRONAS and the Royal Academy of Engineering for a Research Chair in Multiphase Fluid Dynamics, and the EPSRC MEMPHIS (EP/K003976/1) and PREMIERE (EP/T000414/1) Programme Grants. We acknowledge HPC facilities provided by the Research Computing Service (RCS) of Imperial College London for the computing time. D.J. and J.C. acknowledge support through computing time at the Institut du Developpement et des Ressources en Informatique Scientifique (IDRIS) of the Centre National de la Recherche Scientifique (CNRS), coordinated by GENCI (Grand Equipement National de Calcul Intensif) Grant 2022 A0122B06721.

## Appendix

The code has been benchmarked against: i) simulations of Notz & Basaran (2004) on the recoiling of surfactant-free liquid threads, ii) the Rayleigh-Plateau instability model for liquid jets of Plateau (1873), iii) the scaling laws of pinching off threads by Eggers (1993) and Lister & Stone (1998), and iv) the work of Blanchette & Bigioni (2006) on droplet impact at vanishing velocity (droplet coalescence on a flat surface). These validations are found elsewhere, i.e. Constante-Amores *et al.* (2021, 2020*a*).

Figure 13 shows the temporal evolution of the kinetic energy,  $E_k$ , and the conservation of liquid volume for the surfactant-free case ( $Re = 1000$  and  $We = 800$ ) for different mesh resolutions. ‘Mesh-1’ and ‘Mesh-2’ refer to different levels of refinement characterised by  $(386)^3$ , and  $(772)^3$ , respectively. As shown in figure 13a, both levels of refinement accurately reproduce the dynamics at the steady state. Based on these results, we conclude that ‘Mesh-2’ is sufficiently refined to ensure mesh-independent results while providing a good compromise with the computational cost. All the results presented in this paper correspond to a ‘Mesh-2’ mesh.

## REFERENCES

- AGBAGLAH, G. & DEEGAN, R. D. 2014 Growth and instability of the liquid rim in the crown splash regime. *Journal of Fluid Mechanics* **752**, 485–496.
- AGBAGLAH, G., JOSSERAND, C. & ZALESKI, S. 2013 Longitudinal instability of a liquid rim. *Physics of Fluids* **25** (2), 022103.
- ANANTHAKRISHNAN, P. & YEUNG, RONALD W. 1994 Nonlinear interaction of a vortex pair with clean and surfactant-covered free surfaces. *Wave Motion* **19** (4), 343 – 365.
- ASAKI, T. J., THIESSEN, D. B. & MARSTON, P. L. 1995 Effect of an insoluble surfactant on capillary oscillations of bubbles in water: Observation of a maximum in the damping. *Phys. Rev. Lett.* **75**, 4336–4336.
- BATCHVAROV, A., KAHOUADJI, L., CONSTANTE-AMORES, C. R., GONÇALVES, G. F. N., SHIN, S., CHERGUI, J., JURIC, D. & MATAR, O. K. 2020*a* Three-dimensional dynamics of falling films in the presence of insoluble surfactants, arXiv: 2005.12669.
- BATCHVAROV, A., KAHOUADJI, L., MAGNINI, M., CONSTANTE-AMORES, C. R., CRASTER, R. V., SHIN, S., CHERGUI, J., JURIC, D. & MATAR, O. K. 2020*b* Effect of surfactant

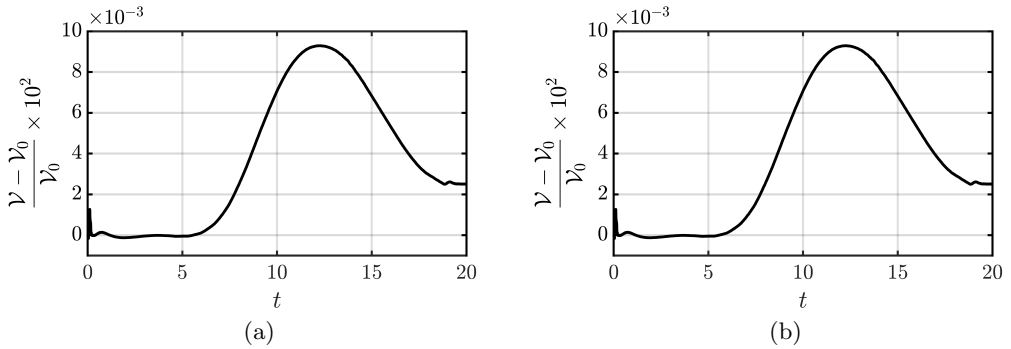


Figure 13: Mesh study for the surfactant-free case when  $Re = 1000$  and  $We = 800$ . The panels highlight the temporal evolution of kinetic energy  $E_k$ , and the relative variation of the liquid volume for two different meshes

- on elongated bubbles in capillary tubes at high reynolds number. *Phys. Rev. Fluids* **5**, 093605.
- BLANCHARD, D. C. & SYZDEK, L. D. 1972 Concentration of bacteria in jet drops from bursting bubbles. *Journal of Geophysical Research (1896-1977)* **77** (27), 5087–5099.
- BLANCHETTE, F. & BIGIONI, T. P. 2006 Partial coalescence of drops at liquid interfaces. *Nature Physics* **2** (4), 254–257.
- CHE, Z. & MATAR, O. K. 2017 Impact of droplets on liquid films in the presence of surfactant. *Langmuir* **33** (43), 12140–12148.
- CHEN, Z., SHU, C., WANG, Y. & YANG, L. M. 2020 Oblique drop impact on thin film: Splashing dynamics at moderate impingement angles. *Physics of Fluids* **32** (3), 033303.
- CHENG, X., SUN, T. P. & GORDILLO, L. 2022 Drop impact dynamics: Impact force and stress distributions. *Annual Review of Fluid Mechanics* **54** (1), null.
- CONSTANTE-AMORES, C.R., KAHOUADJI, L., BATCHVAROV, A., SHIN, S., CHERGUI, J., JURIC, D. & MATAR, O.K. 2021 Direct numerical simulations of transient turbulent jets: vortex-interface interactions. *J. Fluid Mech.* **922**, A6.
- CONSTANTE-AMORES, C. R., CHERGUI, J., SHIN, S., JURIC, D., CASTREJON-PITA, J. R. & CASTREJON-PITA, A. A. 2022 Role of surfactant-induced marangoni stresses in retracting liquid sheets. *arXiv:2202.12167 (accepted)* .
- CONSTANTE-AMORES, C. R., KAHOUADJI, L., BATCHVAROV, A., S., SEUNGWON, CHERGUI, J., JURIC, D. & MATAR, O. K. 2020a Dynamics of retracting surfactant-laden ligaments at intermediate ohnesorge number. *Phys. Rev. Fluids* **5**, 084007.
- CONSTANTE-AMORES, C. R., KAHOUADJI, L., BATCHVAROV, A., SHIN, S., CHERGUI, J., JURIC, D. & MATAR, O. K. 2020b Dynamics of a surfactant-laden bubble bursting through an interface, arXiv: 2005.04472.
- CRASTER, R. V., MATAR, O. K. & PAPAGEORGIOU, D. T. 2002 Pinchoff and satellite formation in surfactant covered viscous threads. *Phys. Fluids* **14** (4), 1364–1376.
- DEEGAN, R D, BRUNET, P & EGGERS, J 2007 Complexities of splashing. *Nonlinearity* **21** (1), C1–C11.
- EDGERTON, H. E. 1977 *Stopping Time: The Photographs of Harold Edgerton*.
- EGGERS, J. 1993 Universal pinching of 3d axisymmetric free-surface flow. *Phys. Rev. Lett.* **71**, 3458–3460.
- FUDGE, B. D., CIMPEANU, R. & CASTREJÓN-PITA, S. A. 2021 Dipping into a new pool: The interface dynamics of drops impacting onto a different liquid. *Phys. Rev. E* **104**, 065102.
- GEKLE, S. & GORDILLO, J. M. 2010 Generation and breakup of worthington jets after cavity collapse. part 1. jet formation. *Journal of Fluid Mechanics* **663**, 293–330.
- GORDILLO, J. M., LHUISSIER, H. & VILLERMAUX, E. 2014 On the cusps bordering liquid sheets. *Journal of Fluid Mechanics* **754**, R1.
- GUEYFFIER, D. & ZALESKI, S. 1998 Formation de digitations lors de l’impact d’une goutte sur un film liquide. *Comptes rendus de l’Académie des sciences.* **326**.

- JOSSERAND, C., RAY, P. & ZALESKI, S. 2016 Droplet impact on a thin liquid film: anatomy of the splash. *Journal of Fluid Mechanics* **802**, 775–805.
- JOSSERAND, C. & THORODDSEN, S.T. 2016 Drop impact on a solid surface. *Annual Review of Fluid Mechanics* **48** (1), 365–391.
- JOSSERAND, C. & ZALESKI, S. 2003 Droplet splashing on a thin liquid film. *Physics of Fluids* **15** (6), 1650–1657.
- KAMAT, P. M., WAGONER, B. W., THETE, S. S. & BASARAN, O. A. 2018 Role of marangoni stress during breakup of surfactant-covered liquid threads: Reduced rates of thinning and microthread cascades. *Phys. Rev. Fluids* **3**, 043602.
- KOVALCHUK, N. M., JENKINSON, H., MILLER, R. & SIMMONS, M. J.H. 2018 Effect of soluble surfactants on pinch-off of moderately viscous drops and satellite size. *J. Colloid Interface Sci.* **516**, 182 – 191.
- KOVALCHUK, N. M. & SIMMONS, M. J.H. 2018 Effect of soluble surfactant on regime transitions at drop formation. *Colloids and Surfaces A: Physicochemical and Engineering Aspects* **545**, 1–7.
- LIANG, G., ZHANG, T., CHEN, Y., CHEN, L. & SHEN, S. 2019 Non-simultaneous impact of multiple droplets on liquid film. *Numerical Heat Transfer, Part A: Applications* **75** (2), 137–147.
- LIAO, Y. C., SUBRAMANI, H. J., FRANSSES, E. I. & BASARAN, O. A. 2004 Effects of soluble surfactants on the deformation and breakup of stretching liquid bridges. *Langmuir* **20** (23), 9926–9930.
- LISTER, J. R. & STONE, H. A. 1998 Capillary breakup of a viscous thread surrounded by another viscous fluid. *Phys. Fluids* **10** (11), 2758–2764.
- MANIKANTAN, H. & SQUIRES, T. M. 2020 Surfactant dynamics: hidden variables controlling fluid flows. *J. Fluid Mech.* **892**, P1.
- NOTZ, P. K. & BASARAN, O. A. 2004 Dynamics and breakup of a contracting liquid filament. *J. Fluid Mech.* **512**, 223–256.
- PLATEAU, J. 1873 *Experimental and Theoretical Statics of Liquids Subject to Molecular Forces Only*, , vol. 1. Gand et Leipzig: F. Clemm.
- REIJERS, STEN A., LIU, BO, LOHSE, DETLEF & GELDERBLUM, HANNEKE 2019 Oblique droplet impact onto a deep liquid pool, arXiv: 1903.08978.
- SHIN, S., CHERGUI, J., JURIC, D., KAHOUADJI, L., MATAR, O. K. & CRASTER, R. V. 2018 A hybrid interface tracking – level set technique for multiphase flow with soluble surfactant. *J. Comp. Phys.* **359**, 409–435.
- STONE, H. A. & LEAL, L. G. 1989 Relaxation and breakup of an initially extended drop in an otherwise quiescent fluid. *Journal of Fluid Mechanics* **198**, 399–427.
- THORAVAL, M. J., TAKEHARA, K., ETOH, TAKEHARU G., POPINET, S., RAY, P., JOSSERAND, C., ZALESKI, S. & THORODDSEN, S. T. 2012 von kármán vortex street within an impacting drop. *Phys. Rev. Lett.* **108**, 264506.
- THORODDSEN, S. T. 2002 The ejecta sheet generated by the impact of a drop. *Journal of Fluid Mechanics* **451**, 373–381.
- THORODDSEN, S. T., THORAVAL, M.-J., TAKEHARA, K. & ETOH, T. G. 2012 Micro-bubble morphologies following drop impacts onto a pool surface. *Journal of Fluid Mechanics* **708**, 469–479.
- WANG, Y. & BOUROUBA, L. 2018 Unsteady sheet fragmentation: droplet sizes and speeds. *Journal of Fluid Mechanics* **848**, 946–967.
- WORTHINGTON, A. M. 1908 *A study of splashes*.
- XAVIER, T., ZUZIO, D., AVERSENG, M. & ESTIVALEZES, J. L. 2020 Toward direct numerical simulation of high speed droplet. *Meccanica* **55** (2), 387–401.
- YARIN, A.L. 2006 Drop impact dynamics: Splashing, spreading, receding, bouncing. . . . *Annual Review of Fluid Mechanics* **38** (1), 159–192.
- ZHANG, L. V., BRUNET, P, EGGERS, J. & DEEGAN, R. D. 2010 Wavelength selection in the crown splash. *Physics of Fluids* **22** (12), 122105.
- ZHANG, L. V., TOOLE, J., FEZZAA, K. & DEEGAN, R. D. 2012 Evolution of the ejecta sheet from the impact of a drop with a deep pool. *Journal of Fluid Mechanics* **690**, 5–15.